Communication: Direct measurements of nascent O(3P0,1,2) fine-structure distributions and branching ratios of correlated spin-orbit resolved product channels CO(ã 3Π; v) + O(3P0,1,2) and CO(X̃ Σ + 1 ; v) + O(3P0,1,2) in VUV photodissociation of CO2

Zhou Lu, Yih Chung Chang, Hong Gao, Yanice Benitez, Yu Song, C. Y. Ng, and W. M. Jackson

Citation: The Journal of Chemical Physics **140**, 231101 (2014); doi: 10.1063/1.4883515
View online: http://dx.doi.org/10.1063/1.4883515
View Table of Contents: http://scitation.aip.org/content/aip/journal/jcp/140/23?ver=pdfcov
Published by the AIP Publishing

Communication: Direct measurements of nascent $O(^3P_{0,1,2})$ fine-structure distributions and branching ratios of correlated spin-orbit resolved product channels $CO(\tilde{a}^3\Pi; v) + O(^3P_{0,1,2})$ and $CO(\tilde{X}^1\Sigma^+; v) + O(^3P_{0,1,2})$ in VUV photodissociation of CO_2

Zhou Lu, Yih Chung Chang, Hong Gao, Yanice Benitez, Yu Song, C. Y. Ng,[a] and W. M. Jackson[a]
Department of Chemistry, University of California, Davis, Davis, California 95616, USA

(Received 16 April 2014; accepted 3 June 2014; published online 17 June 2014)

We present a generally applicable experimental method for the direct measurement of nascent spin-orbit state distributions of atomic photofragments based on the detection of vacuum ultraviolet (VUV)-excited autoionizing-Rydberg (VUV-EAR) states. The incorporation of this VUV-EAR method in the application of the newly established VUV-VUV laser velocity-map-imaging-photoion (VMI-PI) apparatus has made possible the branching ratio measurement for correlated spin-orbit state resolved product channels, $CO(\tilde{a}^3\Pi; v) + O(^3P_{0,1,2})$ and $CO(\tilde{X}^1\Sigma^+; v) + O(^3P_{0,1,2})$, formed by VUV photoexcitation of CO_2 to the $4s(1_0{}^1)$ Rydberg state at 97,955.7 cm^{-1}. The total kinetic energy release (TKER) spectra obtained from the O^+ VMI-PI images of $O(^3P_{0,1,2})$ reveal the formation of correlated $CO(\tilde{a}^3\Pi; v = 0–2)$ with well-resolved $v = 0–2$ vibrational bands. This observation shows that the dissociation of CO_2 to form the spin-allowed $CO(\tilde{a}^3\Pi; v = 0–2) + O(^3P_{0,1,2})$ channel has no potential energy barrier. The TKER spectra for the spin-forbidden $CO(\tilde{X}^1\Sigma^+; v) + O(^3P_{0,1,2})$ channel were found to exhibit broad profiles, indicative of the formation of a broad range of rovibrational states of $CO(\tilde{X}^1\Sigma^+)$ with significant vibrational populations for $v = 18–26$. While the VMI-PI images for the $CO(\tilde{a}^3\Pi; v = 0–2) + O(^3P_{0,1,2})$ channel are anisotropic, indicating that the predissociation of CO_2 $4s(1_0{}^1)$ occurs via a near linear configuration in a time scale shorter than the rotational period, the angular distributions for the $CO(\tilde{X}^1\Sigma^+; v) + O(^3P_{0,1,2})$ channel are close to isotropic, revealing a slower predissociation process, which possibly occurs on a triplet surface via an intersystem crossing mechanism. © *2014 AIP Publishing LLC*. [http://dx.doi.org/10.1063/1.4883515]

Carbon dioxide (CO_2) plays an important role in the Earth's atmosphere as one of the main greenhouse gases. It is also the most abundant molecular species (≈95%) in the atmospheres of Mars and Venus.[1] The observation of the $CO(\tilde{a}^3\Pi - \tilde{X}^1\Sigma^+)$ Cameron emission bands from comets also suggests that CO_2 exists in abundance in comets.[2] Solar vacuum ultraviolet (VUV) photodissociation is considered to be a major sink for CO_2 in the thermosphere. Thus, the detailed investigation of CO_2 photodissociation over a wide VUV range of wavelengths is of paramount importance for reliable modeling of the photochemistry occurring in the atmospheres of early Earth,[3] Mars,[4] and Venus.[5]

Due to the availability of high-power F_2 lasers, previous VUV photodissociation studies of CO_2 have been focused on the formation of the spin-forbidden $CO(\tilde{X}^1\Sigma^+; v) + O(^3P_J)$ channel at 157 nm.[6–10] The branching ratios of the $O(^3P)$ and $O(^1D)$ exit channels at 157 nm have also been examined by Zhu and Gordon[7] and Stolow and Lee.[9] The determination of $O(^3P_{0,1,2})$ fine structure distribution provides some of the most detailed information about the dynamics of CO_2 photodissociation. Matsumi *et al.* measured a non-statistical $O(^3P_{0,1,2})$ fine structure distribution for the CO_2 photodissociation at 157 nm by using an ultraviolet (UV) laser (2+1) resonance-enhanced multiphoton ionization (REMPI) scheme.[8] Recently, Chen *et al.* investigated the correlated formation of $O(^3P_{0,1,2})$ with $CO(\tilde{X}^1\Sigma^+; v)$ from CO_2 photodissociation at 157 nm by employing the velocity-map imaging-photoion (VMI-PI) method.[6] Although the O^+ VMI-PI images from (2+1) REMPI of $O(^3P_{0,1,2})$ were measured, the $O(^3P_{0,1,2})$ fine structure distribution was not reported. The major difficulty involved in fine structure distribution measurements using the UV laser (2+1) REMPI scheme is that the two-photon absorption cross section for forming the intermediate state and the photoionization cross sections from this intermediate state are not known. Because of the small cross sections for two-photon absorption, it is necessary to focus the UV laser to increase the sensitivity for (2+1) REMPI detection. This can introduce a significant uncertainty in determining the branching for the different $O(^3P_{0,1,2})$ spin-orbit states.

While the CO_2 absorption cross sections are very weak at VUV energies below 11.0 eV,[11] they are significantly higher in the VUV range of 11.0–14.0 eV. Thus, it is desirable to examine the photochemistry of CO_2 at this energy range. Lawrence recorded the fractional yield of the $CO(\tilde{a}^3\Pi - \tilde{X}^1\Sigma^+)$ Cameron band emission induced by VUV photodissociation of CO_2, and it reveals a smooth increase for the formation of the spin-allowed $CO(\tilde{a}^3\Pi) + O(^3P)$

[a]Authors to whom correspondence should be addressed. Electronic addresses: cyng@chem.ucdavis.edu and wmjackson@ucdavis.edu

channel from its thermochemical threshold at 11.46 eV to a maximum value of 50%–60% near 13.78 eV.[12] Very recently, Song *et al.* performed a detailed study of the VUV photochemistry of CO_2 in the VUV energy of 13.540–13.678 eV using the VUV laser time-slice VMI-PI method together with a (2+1) REMPI scheme for $O(^3P_{0,1,2})$ detection.[13] They were able to identify nearly all energetically accessible photoproduct channels but did not determine the $O(^3P_{0,1,2})$ fine structure distributions. For the state-resolved photodissociation results to be useful for atmospheric modeling and for rigorous comparisons with first-principle theoretical calculations, it is most important to determine accurate branching ratios for the accessible photoproduct channels.

In this Communication, we present a sensitive and generally applicable experimental scheme for the direct determination of $O(^3P_{0,1,2})$ spin-orbit state distributions produced by VUV photodissociation of CO_2 based on the detection of VUV-excited autoionizing Rydberg (VUV-EAR) states. By using this VUV-EAR method along with time-slice VMI-PI measurements, we have determined the branching ratios for the correlated spin-orbit resolved product channels, $CO(\tilde{X}^1\Sigma^+) + O(^3P_{0,1,2})$ and $CO(\tilde{a}^3\Pi) + O(^3P_{0,1,2})$, formed by VUV photoexcitation of CO_2 to the $4s(1_0^1)$ Rydberg state at 97 955.7 cm^{-1}. This VUV-EAR method is found to exhibit superior detection sensitivity compared to the UV 2+1 REMPI scheme due to the larger photoionization volume used and the higher one photon VUV excitation cross section.

A detailed description of the VUV-VUV laser time-slice VMI-PI apparatus used in the present experiment has been reported previously.[13–16] The CO_2 sample (10% CO_2 in He) is introduced into the photoionization/photoexcitation (PI/PEX) region in the form of a pulsed (30 Hz) supersonic beam. Two independently tunable VUV lasers, designated as VUV-I for photodissociation pump and VUV-II for photoionization probe, are used. Both VUV-I and VUV-II have the same design and are generated by four-wave sum-frequency mixing schemes, providing a tunable VUV output of interest equals to $(2\omega_1+\omega_2)$ by using Xe or Kr as the nonlinear medium.[17] Here, ω_1 and ω_2 represent the respective ultraviolet (UV) and visible (VIS) fundamental outputs of the tunable dye lasers. Since no dispersive devise was used to separate the sum-frequency $(2\omega_1+\omega_2)$ from the difference-frequency $(2\omega_1-\omega_2)$, the triple frequency $3\omega_1$, and the fundamental frequencies ω_1 and ω_2, all these frequencies entered the PI/PEX center as the VUV-I and VUV-II beams to intersect the CO_2 molecular beam. A retractable LiF (or MgF_2) window can be inserted in the path of the VUV-I or VUV-II beam to block the VUV sum-frequency. By comparing the O^+ ion signals observed with and without the $(2\omega_1 + \omega_2)$ frequencies, we conclude that photodissociation of CO_2 and photoionization of $O(^3P_{0,1,2})$ observed here are induced by absorption of the VUV sum-frequencies with little contamination from other VUV and fundamental outputs. The relative intensities for the VUV sum-frequencies of interest were measured by using the photoionization efficiency spectrum of C_2H_2,[20] which is recorded in situ during the experiment. The photodissociation and photoionization yields presented here have all been normalized by the corresponding VUV intensities.

In a previous experiment, we have reported on the successful determination of $C(^3P_{0,1,2})$ fine-structure distributions based on the two-color VUV-VIS $(1 + 1')$ photoionization method.[14] The success of this experiment on $C(^3P_{0,1,2})$ prompted us to seek a similar experimental scheme for measuring the $O(^3P_{0,1,2})$ fine-structure distribution. A survey of the available O atom Rydberg states lying below the IE(O) at 13.618 eV suggests that $O(^3P_{0,1,2})$ photofragments can be efficiently detected by the VUV-VIS $(1 + 1')$ REMPI scheme via the intermediate Rydberg states $O^*[2s^22p^3(^4S^\circ)3d\ (^3D^\circ_{1,2,3})]$. As shown in the left panel of Fig. 1, the first step (shown by blue arrows) of this scheme involved the excitation of $O(^3P_0)$, $O(^3P_1)$, and $O(^3P_2)$ to the common intermediate state $O^*[2s^22p^3(^4S^\circ)3d\ (^3D^\circ_1)]$ by setting VUV-II at 97 261.40, 97 330.11, and 97 488.38 cm^{-1}, respectively. Since the second photoionization steps (shown by red arrows in Fig. 1), which involves photoexcitation from this intermediate Rydberg state to the ionization continuum by the absorption of a visible photon at 2.13 eV in this study, have the same cross section, the nascent populations for $O(^3P_{0,1,2})$ can be determined based on the measured O^+ ion intensities from $O(^3P_{0,1,2})$ and the known cross sections of the first VUV excitation steps. However, due to the small energy separations of the $O^*[2s^22p^3(^4S^\circ)3d\ (^3D^\circ_{1,2,3})]$ spin-orbit states, the transition energies from $O(^3P_2)$ to these states differ only by $\leq$0.16 cm^{-1} and those from $O(^3P_1)$ to $O^*[2s^22p^3(^4S^\circ)3d\ (^3D^\circ_{1,2})]$ by $\leq$0.07 cm^{-1}. These small energy separations do not allow individual transitions to be resolved by using the VUV-II laser. The actual observed transition energies for $O(^3P_2) \rightarrow O^*[2s^22p^3(^4S^\circ)3d\ (^3D^\circ_{1,2,3})]$, $O(^3P_1) \rightarrow O^*[2s^22p^3\ (^4S^\circ)3d\ (^3D^\circ_{1,2})]$, and $O(^3P_0) \rightarrow O^*[2s^22p^3(^4S^\circ)3d\ (^3D^\circ_1)]$ are found to be at 97 489.9, 97 331.7, and 97 262.6 cm^{-1}, respectively. Although these Rydberg states $O^*[2s^22p^3(^4S^\circ)3d\ (^3D^\circ_{1,2,3})]$ cannot be used for the direct determination of the $O(^3P_{0,1,2})$ fine structure distribution due to the unresolved excitations, it can serve to

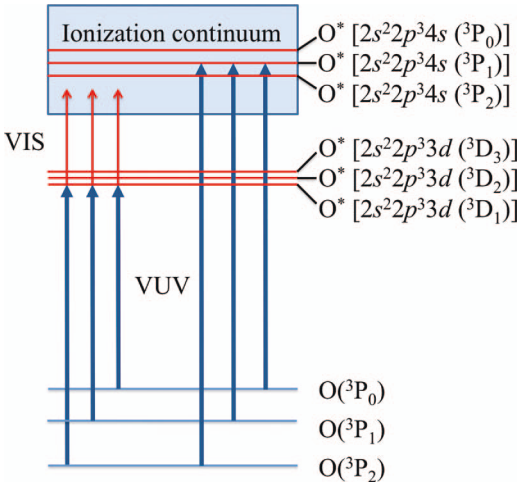

FIG. 1. Schematic diagram illustrating the spin-orbit-state selective detection schemes for $O(^3P_0)$, $O(^3P_1)$, and $O(^3P_2)$. The two-color VUV-VIS $(1 + 1')$ REMPI and the VUV-EAR schemes are shown on the left and right panels, respectively. The Rydberg states $O^*[2s^22p^3(^4S^\circ)3d\ (^3D^\circ_{1,2,3})]$ and $O^*[2s^22p^3(^2P^\circ)4s\ (^3P^\circ_{0,1,2})]$ are chosen as the intermediate states for VUV-VIS $(1 + 1')$ REMPI and VUV-EAR detection, respectively.

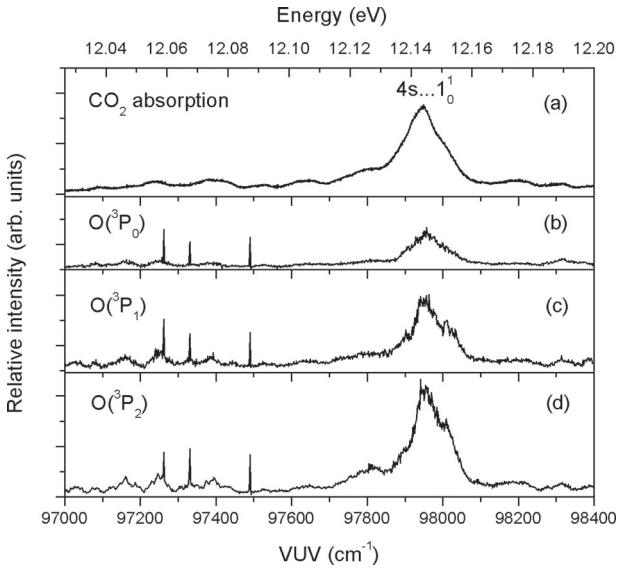

FIG. 2. Comparison of (a) the absorption spectrum of CO_2 and the O^+ PHOFEX spectra of (b) $O(^3P_0)$, (c) $O(^3P_1)$, and (d) $O(^3P_2)$ formed by the photodissociation of CO_2 in the range of 97 000–98 400 cm^{-1}. The PHOFEX spectra of $O(^3P_0)$, $O(^3P_1)$, and $O(^3P_2)$ were obtained by setting VUV-II at 97 262.6, 97 331.7 and 97 489.9 cm^{-1}, and scan VUV-I in the range of 97 000–98 400 cm^{-1}.

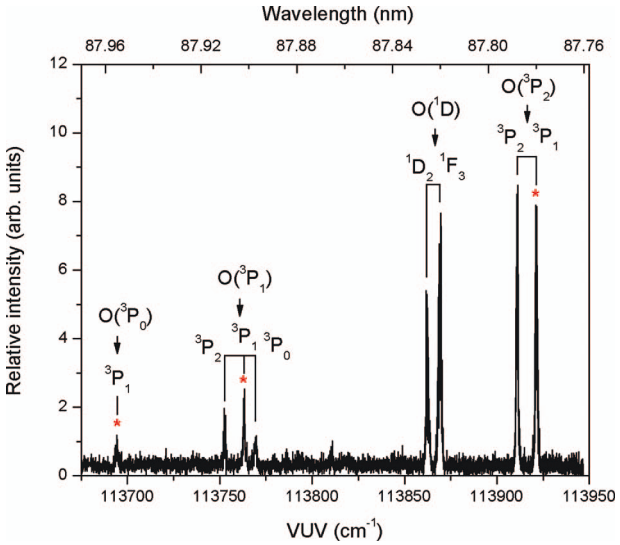

FIG. 3. The O^+ ion spectrum observed by VUV-II excitations, $O(^3P_{0,1,2}) \rightarrow O^*[2s^22p^3(^2P^\circ)4s\ (^3P^\circ_{0,1,2})]$ and $O(^1D_2) \rightarrow O^*[2s^22p^3(^2D^o_{3/2})4d\ (^1D^o_2)]$ and $O^*[2s^22p^3(^2D^o_{3/2})4d\ (^1F^o_3)]$ in the energy range of 113 675–113 950 cm^{-1}. Here, $O(^3P_J)$ and $O(^1D_2)$ are products of VUV photodissociation of CO_2 at 97 955.7 cm^{-1}. The excitation transitions to the common $O^*[2s^22p^3(^2P^\circ)3s\ (^3P^\circ_1)]$ state from $O(^3P_0)$ $O(^3P_1)$ and $O(^3P_2)$ are highlighted by red asterisks.

provide an efficient detection scheme for the $O(^3P_{0,1,2})$ spin-orbit states. By setting VUV-II at 97 262.6, 97 331.7, and 97 489.9 cm^{-1}, and scan VUV-I in the range of 97 000–98 400 cm^{-1} (12.03–12.20 eV), we have obtained the O^+ photofragment excitation (PHOFEX) spectra of $O(^3P_0)$, $O(^3P_1)$, and $O(^3P_2)$ as shown in Figs. 2(b)–2(d), respectively. The structures of these PHOFEX spectra are in excellent agreement with the high-resolution absorption spectrum of CO_2 [shown in Fig. 2(a)] that was previously reported by Cossart-Magos *et al.*[18] and Archer *et al.*[19] The strongest absorption peak centered at 97 955.7 cm^{-1} is assigned to the $CO_2[4s(1_0^1)]$ Rydberg band. Three sharp O^+ ion peaks at 97 262.6, 97 331.7, and 97 489.9 cm^{-1} are evident in the PHOFEX spectra that result from the increase of O^+ ion yields by VUV-VIS $(1 + 1')$ REMPI of $O(^3P_{0,1,2})$ induced by VUV-I excitation. This observation illustrates the high sensitivity of the VUV-VIS $(1 + 1')$ REMPI scheme for $O(^3P_{0,1,2})$ detection.

The VUV-EAR scheme used for the direct determination of the $O(^3P_{0,1,2})$ fine structure distribution in the present study is shown in the right panel of Fig. 1, which requires only a single excitation step (shown by blue arrows), i.e., the direct VUV-II excitation of $O(^3P_{0,1,2})$ to a common Rydberg state $O^*[2s^22p^3(^2P^\circ)4s\ (^3P^\circ_1)]$ located at 113 921.39 cm^{-1} (14.124 eV) lying above the IE(O) = 13.618 eV. The O^+ ion intensity produced by autoionizing of this common Rydberg state is thus only dependent upon the nascent populations of the $O(^3P_{0,1,2})$ spin-orbit states and the cross sections for the VUV-II excitation transitions, which are known by close coupling calculations.[21] Figure 3 depicts the observed O^+ ion intensities induced by the VUV-II excitations $O(^3P_{0,1,2}) \rightarrow O^*[2s^22p^3(^2P^\circ)4s\ (^3P^\circ_{0,1,2})]$ in the energy range of 113 675–113 950 cm^{-1}. The observed O^+ ion peaks are assigned to dipole allowed transitions as marked in Fig. 3. The three excitation transitions to the intermediate Rydberg state $O^*[2s^22p^3(^2P^\circ)3s\ (^3P^\circ_1)]$ from $O(^3P_0)$ $O(^3P_1)$, and $O(^3P_2)$ are highlighted by red asterisks. The integrated areas of the $O(^3P_0)$, $O(^3P_1)$, and $O(^3P_2)$ are used to determine the intensity associated with formation of each of these spin-orbit states from the photodissociation of CO_2 in the $4s(1_0^1)$ state. After correcting for the calculated transition probabilities of 2.26×10^8, 1.7×10^8, and 2.85×10^8 for the transitions from $O(^3P_0)$, $O(^3P_1)$, and $O(^3P_2)$ to $O^*[2s^22p^3(^2P^\circ)3s\ (^3P^\circ_1)]$,[21] respectively, we obtained the nascent distribution $O(^3P_0)$: $O(^3P_1)$: $O(^3P_2)$ = 0.12(2): 0.25(3): 0.63(2). The uncertainty assigned to this distribution reflects the maximum deviation observed in more than three independent measurements. Comparing this distribution to the statistical distribution of 0.11: 0.33: 0.56 obtained using the 2J+1 degeneracy of the M_J levels, we find that the distribution obtained here is colder with a slightly higher populations for the ground $O(^3P_2)$ state. We note that $CO(\tilde{X}^1\Sigma^+;\ v) + O(^1D_2)$ is also an open product channel from $CO_2[4s(1_0^1)]$ predissociation. The O^+ ion peaks originated from excitations of $O(^1D_2)$ to the autoionizing Rydberg state $O^*[2s^22p^3(^2D^o_{3/2})4d\ (^1D^o_2)]$ and $O^*[2s^22p^3(^2D^o_{3/2})4d\ (^1F^o_3)]$ are also identified in this VUV-II energy range as marked in Fig. 3.

Figures 4(a)–4(c) depict the time-slice O^+ VMI-PI images of $O(^3P_0)$, $O(^3P_1)$, and $O(^3P_2)$ produced by photodissociation of CO_2 with VUV-I set at exciting the $CO_2[4s(1_0^1)]$ Rydberg state. The corresponding TKER spectra obtained from these images are shown in Figs. 4(d)–4(f). On the basis of the known energetics and vibrational constants of $CO(\tilde{a}^3\Pi)$ and $CO(\tilde{X}^1\Sigma^+)$, the TKER spectra for the $CO(\tilde{a}^3\Pi) + O(^3P_{0,1,2})$ and the $CO(\tilde{X}^1\Sigma^+) + O(^3P_{0,1,2})$ channels are simulated as shown by the red and the blue curves, respectively. The simulation is guided by the trend of the measured

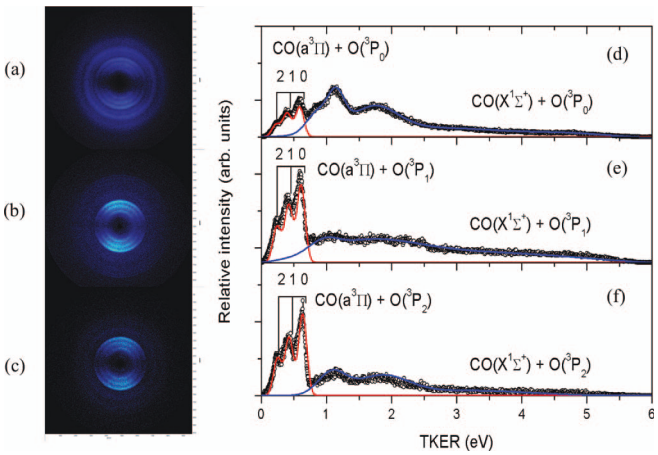

FIG. 4. Time-slice O^+ VMI-PI images for (a) $O(^3P_0)$, (b) $O(^3P_1)$, and (c) $O(^3P_2)$ produced by photodissociation of CO_2 with VUV-I set at the $CO_2[4s(1_0{}^1)]$ Rydberg state. The corresponding TKER spectra obtained from these images are shown in (d), (e) and (f). The TKER spectra for the $CO(\tilde{a}^3\Pi) + O(^3P_{2,1,0})$ and the $CO(\tilde{X}^1\Sigma^+) + O(^3P_{2,1,0})$ channels are simulated as shown by the red and the blue curves, respectively.

TKER spectra. Since the red and blue curves overlap, it is necessary to separate the contribution by the spin-allowed and spin-forbidden channels in the overlap region by simulation in order to determine the branching ratios for these product channels. The uncertainties introduced by the simulation were included in the error limit assigned for the branching ratios reported here. The three sharp, anisotropic inner rings of the VMI-PI images correspond to the formation of the v = 0–2 vibrational states of the spin-allowed $CO(\tilde{a}^3\Pi; v) + O(^3P_J)$ channel as marked on top of the red TKER spectra. The observation of the correlated formation of $CO(\tilde{a}^3\Pi; v = 0–2)$ and $O(^3P_{0,1,2})$ indicates that there is no energy barrier for the formation of the spin-allowed $CO(\tilde{a}^3\Pi) + O(^3P_J)$ channel. The resolved vibrational structures for $CO(\tilde{a}^3\Pi; v = 0–2)$ is indicative of a relatively low rotational excitation for $CO(\tilde{a}^3\Pi; v = 0–2)$ resulting from a prompt dissociation mechanism via a near linear O-C-O configuration. The outer rings of the VMI-PI images of Figs. 4(a)–4(c) exhibit broad, near isotropic structures, which are transformed into the relatively smooth blue TKER spectra for the formation of the spin-forbidden $CO(\tilde{X}^1\Sigma^+; v) + O(^3P_{0,1,2})$ channel as shown in Figs. 4(d)–4(f). The smooth TKER profiles can be partly ascribed to a high rotational excitation and a wide Doppler profile of $O(^3P_{0,1,2})$ recoils resulting from the high exothermicity for the spin-forbidden channel. The TKER measurement for the $CO(\tilde{X}^1\Sigma^+; v) + O(^3P_{0,1,2})$ channel also reveals the formation of a broad range of rovibrational states $CO(\tilde{X}^1\Sigma^+; v \leq 30)$ with significant populations for v = 18–26. The high vibrational excitation for this product channel was also observed previously in the 157 nm photodissociation of CO_2.[6]

We have determined the anisotropy β parameters based on the analysis of the time-slice VMI-PI images for the $CO(\tilde{a}^3\Pi; v = 0–2) + O(^3P_{0,1,2})$ and $CO(\tilde{X}^1\Sigma^+) + O(^3P_{0,1,2})$ product channels from the predissociation of $CO_2[4s(1_0{}^1)]$. The β parameter was found to decrease with increasing vibrational excitation of $CO(\tilde{a}^3\Pi)$ and spin-orbit excitation of $O(^3P_J)$ and fall in the range of 1.0–1.8. For the $CO(\tilde{a}^3\Pi; v = 0) + O(^3P_J)$ (J = 0, 1, and 2) channels, the β parameters have the respective values of 1.0(2), 1.6(2), and 1.8(1). The change in the β parameter with J implies that the $O(^3P_{0,1,2})$ spin-orbit states form at different rates. The fastest dissociation occurs for the ground $O(^3P_2)$ state, while the slowest dissociation takes place for the excited $O(^3P_0)$ state that is 227.98 cm^{-1} above the ground $O(^3P_2)$ state. The $\beta = 1.8$ obtained for the $CO(\tilde{a}^3\Pi) + O(^3P_2)$ product channel indicates a near parallel transition of this channel, and a Σ symmetry for the CO_2 $4s(1_0{}^1)$ Rydberg state. The anisotropy β parameters obtained from the outer broad ring structures are 0.52(5), 0.27(3), and 0.37(7) for the respective $O(^3P_0)$, $(^3P_1)$, and $(^3P_2)$ VMI-PI images. These β values correspond to near isotropic angular distributions for the spin-forbidden product channel. This observation is consistent with a slower photodissociation mechanism for the spin-forbidden channel via the triplet potential energy surface with a dissociation lifetime comparable to the rotational period of excited CO_2. The smaller β parameters observed for vibrational and spin-orbit excitations may be ascribed to a more efficient singlet-triplet coupling. The *ab initio* calculation of Hwang and Mebel on CO_2 dissociation predicts that the spin-forbidden $CO(\tilde{X}^1\Sigma^+) + O(^3P_J)$ channel is produced via the triplet potential energy structure of $^3A'$ electronic symmetry, which has one extended C-O bond, while the other C-O bond is compressed in a bent OCO geometry, leading to the formation of rovibrationally excited $CO(\tilde{X}^1\Sigma^+)$ photoproducts.[22]

By integrating the areas under the red and blue TKER curves of Figs. 4(d)–4(f), we have determined the branching ratios, $CO(\tilde{a}^3\Pi; v = 0–2) + O(^3P_J)$: $CO(\tilde{X}^1\Sigma^+; v \leq 30) + O(^3P_J)$ for J = 0, 1, and 2, to be 0.16(2): 0.84(2), 0.25(2): 0.75(2), and 0.34(3): 0.66(3), respectively. These ratios show that the branching fraction for the spin-allowed channel increases as J is increased. The $CO(\tilde{a}^3\Pi; v = 0–2) + O(^3P_J)$ channel is observed to have a smaller branching ratio compared to the $CO(\tilde{X}^1\Sigma^+) + O(^3P_J)$ channel from $CO_2[4s(1_0{}^1)]$ predissociation. The normalization of these branching ratios for $CO(\tilde{a}^3\Pi) + O(^3P_J)$: $CO(\tilde{X}^1\Sigma^+) + O(^3P_J)$ (J = 0, 1, and 2) by the fine structure distribution $O(^3P_0)$: $O(^3P_1)$: $O(^3P_2)$ = 0.12(2): 0.25(3): 0.63(2) measured in the present study have enabled the determination of the branching ratios for the correlated spin-orbit state resolved product channels, $CO(\tilde{a}^3\Pi; v = 0–2) + O(^3P_0)$: $CO(\tilde{a}^3\Pi; v = 0–2) + O(^3P_1)$: $CO(\tilde{a}^3\Pi; v = 0–2) + O(^3P_2)$: $CO(\tilde{X}^1\Sigma^+; v \leq 30) + O(^3P_0)$: $CO(\tilde{X}^1\Sigma^+; v \leq 30) + O(^3P_1)$: $CO(\tilde{X}^1\Sigma^+; v \leq 30) + O(^3P_2)$ = 0.019(4): 0.063(9): 0.21(2): 0.10(2): 0.19(2): 0.42(2). These quantitative experimental measurements are expected to be useful for modeling the photochemistry occurring in planetary atmospheres as well as providing a benchmark for comparison with rigorous first-principle theoretical predictions on the photodissociation dynamics of CO_2.

C.Y.N was supported by the U.S. Department of Energy (DOE) Contract No. DE-FG02-02ER15306. W.M.J was supported the NSF Grant No. CHE-1301501. We also thank Dr. Glenn Stark for providing the digitized CO_2 photoabsorption spectrum.

[1]J. Levine, *The Photochemistry of Atmospheres* (Elsevier, 1985).
[2]K. S. Kalogerakis, C. Romanescu, M. Ahmed, K. R. Wilson, and T. G. Slanger, Icarus **220**, 205 (2012).
[3]J. Haqq-Misra, J. F. Kasting, and S. Lee, Astrobiology **11**, 293 (2011).
[4]A. Anbar, M. Allen, and H. Nair, J. Geophys. Res. **98**, 10925, doi:10.1029/93JE00330 (1993).
[5]M. B. McElroy, N. Dak Sze, and Y. Ling Yung, J. Atmos. Sci. **30**, 1437 (1973).
[6]Z. Chen, F. Liu, B. Jiang, X. Yang, and D. H. Parker, J. Phys. Chem. Lett. **1**, 1861 (2010).
[7]I. Lu, J. J. Lin, S.-H. Lee, Y. T. Lee, and X. Yang, Chem. Phys. Lett. **382**, 665 (2003).
[8]Y. Matsumi, N. Shafer, K. Tonokura, M. Kawasaki, Y.-L. Huang, and R. J. Gordon, J. Chem. Phys. **95**, 7311 (1991).
[9]A. Stolow and Y. T. Lee, J. Chem. Phys. **98**, 2066 (1993).
[10]Y. F. Zhu and R. J. Gordon, J. Chem. Phys. **92**, 2897 (1990).
[11]W. Chan, G. Cooper, and C. Brion, Chem. Phys. **178**, 401 (1993).
[12]G. M. Lawrence, J. Chem. Phys. **56**, 3435 (1972).
[13]Y. Song, H. Gao, Y. C. Chang, Z. Lu, C. Y. Ng, and W. M. Jackson, Phys. Chem. Chem. Phys. **16**, 563 (2014).
[14]H. Gao, Y. Song, W. M. Jackson, and C. Y. Ng, J. Chem. Phys. **138**, 191102 (2013).
[15]Y. Pan, H. Gao, L. Yang, J. Zhou, C. Y. Ng, and W. M. Jackson, J. Chem. Phys. **135**, 071101 (2011).
[16]J. Zhou, K. C. Lau, E. Hassanein, H. Xu, S. X. Tian, B. Jones, and C. Y. Ng, J. Chem. Phys. **124**, 034309 (2006).
[17]C. Y. Ng, Annu. Rev. Phys. Chem. **53**, 101 (2002).
[18]C. Cossart-Magos, M. Jungen, and F. Launay, Mol. Phys. **61**, 1077 (1987).
[19]L. Archer, G. Stark, P. Smith, J. Lyons, N. de Oliveira, L. Nahon, D. Joyeux, and D. Blackie, J. Quant. Spectrosc. Radiat. Transfer **117**, 88 (2013).
[20]V. H. Dibeler and J. A. Walker, Int. J. Mass Spectrom. Ion Phys. **11**, 49 (1973).
[21]K. Butler and C. Zeippen, J. Phys. IV **1**, C1 (1991).
[22]D. Y. Hwang and A. M. Mebel, Chem. Phys. **256**, 169 (2000).